

The GIRAFFE Inner Bulge Survey (GIBS) III. Metallicity distributions and kinematics of 26 Galactic bulge fields [★]

M. Zoccali^{1,2}, S. Vasquez^{1,2}, O. A. Gonzalez³, E. Valenti⁴, A. Rojas-Arriagada^{2,1}, J. Minniti^{1,2}, M. Rejkuba^{4,5}, D. Minniti^{6,2,7}, A. McWilliam⁸, C. Babusiaux⁹, V. Hill¹⁰, and A. Renzini¹¹

¹ Instituto de Astrofísica, Pontificia Universidad Católica de Chile, Av. Vicuña Mackenna 4860, 782-0436 Macul, Santiago, Chile
e-mail: mzoccali@astro.puc.cl

² Millennium Institute of Astrophysics, Av. Vicuña Mackenna 4860, 782-0436 Macul, Santiago, Chile

³ UK Astronomy Technology Centre, Royal Observatory, Blackford Hill, Edinburgh, UK

⁴ European Southern Observatory, Karl-Schwarzschild Strasse 2, D-85748 Garching, Germany

⁵ Excellence Cluster Origin and Structure of the Universe, Boltzmannstr. 2, D-85748 Garching bei München, Germany Departamento de Ciencias Físicas, Universidad Andrés Bello, 220 República, Santiago, Chile

⁶ Departamento de Física, Facultad de Ciencias Exactas, Universidad Andres Bello Av. Fernandez Concha 700, Las Condes, Santiago, Chile

⁷ Vatican Observatory, V00120 Vatican City State, Italy

⁸ The Observatories of the Carnegie Institution of Washington, 813 Santa Barbara St., Pasadena, CA 91101–1292

⁹ GEPI, Observatoire de Paris, CNRS UMR 8111, Université Paris Diderot, F-92125, Meudon, Cedex, France

¹⁰ Université de la Côte d’Azur, Observatoire de la Côte d’Azur, CNRS, Laboratoire Lagrange, Bd de l’Observatoire, CS 34229, 06304 Nice Cedex 4, France

¹¹ INAF - Osservatorio Astronomico di Padova, vicolo dell’Osservatorio 5, 35122, Padova, Italy

October 31, 2016

ABSTRACT

Context. Several recent studies have demonstrated that the Galactic bulge hosts two components with different mean metallicities, and possibly different spatial distribution and kinematics. As a consequence, both the metallicity distribution and the radial velocity of bulge stars vary across different line of sights.

Aims. We present here the metallicity distribution function of red clump stars in 26 fields spread across a wide area of the bulge, with special emphasis on fields close to Galactic plane, at latitudes $b = -2^\circ$ and $b = -1^\circ$, that were not explored before.

Methods. This paper includes new metallicities from a sample of ~ 5000 K giant stars, observed at spectral resolution $R \sim 6500$, in the Calcium II Triplet region. They are the main dataset of the GIRAFFE Inner Bulge Survey. As part of the same survey we have previously published results for a sample of ~ 600 K giant stars, at latitude $b \sim -4^\circ$, derived from higher resolution spectra ($R=22,500$).

Results. The combined sample allows us to trace and characterize the metal poor and metal rich bulge populations down to the inner bulge. We present a density map for each of the two components. Contrary to the expectations from previous works, we found the metal poor population to be more centrally concentrated than the metal rich one, and with a more axisymmetric spatial distribution. The metal rich population, on the other hand, is arranged in a boxy distribution, consistent with an edge-on bar. By coupling metallicities and radial velocities we show that the metal poor population has a velocity dispersion that varies rather mildly with latitude. On the contrary, the metal rich population has a low velocity dispersion far from the plane ($b = -8.5^\circ$), but it has a steeper gradient with latitude, becoming higher than the metal poor one in the innermost field ($b = -1^\circ$).

Conclusions. This work provides new observational constraints on the actual chemodynamical properties of the Galactic bulge, that will help discriminating among different formation models.

Key words. Stars: abundances – Galaxy: bulge – Galaxy: structure – Galaxy: kinematics and dynamics – Galaxy: stellar content –

1. Introduction

Until a decade ago, our knowledge about the properties of the Galactic bulge, the second most massive component of the Milky Way, was relatively poor. Yet we thought we knew most of what was relevant. We knew it was an elongated spheroid (i.e., a bar Stanek et al. 1994), with a broad metallicity distribution (Rich 1988), containing mostly old stars (Ortolani et al. 1995). The results of the investigations cited above were refined by several other authors (e.g. McWilliam & Rich 1994; Zoccali et al. 2003)

but none of them covered a wide area of the bulge, thus the common belief was that the bulge was a rather uniform population.

Wide area photometric and spectroscopic surveys conducted in the last 10 years revealed that the bulge is much more complex.

Concerning the bulge three dimensional structure, we now know that the bar flares up in a boxy/peanut, or X-shape (McWilliam & Zoccali 2010; Nataf et al. 2010; Saito et al. 2011; Wegg & Gerhard 2013), unequivocal signature of a formation scenario starting from a disk, whose dynamical instabilities funnel stars, and maybe gas, towards the center forming a bar, which later bends and buckles giving rise to the X-shape (Patsis et al. 2002; Athanassoula 2005). However we also know that the old-

[★] Based on observations taken with ESO telescopes at the La Silla Paranal Observatory under programme IDs 71.B-0617, 385.B-0735 and 187.B-0909

est and more metal poor stars do not follow the same structure. In fact, RR Lyrae trace a more axisymmetric component, compared with the RC (Dékány et al. 2013; Pietrukowicz et al. 2015). Also, metal poor red clump (RC) stars do not trace the X-shape (Ness et al. 2012; Rojas-Arriagada et al. 2014). Furthermore, there is evidence for an axisymmetric structure within the inner 250pc of the bulge (Gonzalez et al. 2011a; Gerhard & Martinez-Valpuesta 2012) and for a thin extension of the bar, called the *long* bar (Wegg et al. 2015, and references therein). A recent review of the 3D structure of the Galactic bulge can be found in (Zoccali & Valenti 2016).

Another fundamental characteristic of any stellar system is the metallicity distribution function (MDF); indeed, stellar systems may be differentiated by their mean metallicity, or $[\text{Fe}/\text{H}]$, and by the metallicity dispersion. At any moment, the gas-phase metal content consists of the integral of the nucleosynthetic yields of the preceding history of star formation, resulting in an increase of the mean metallicity with time. The observed MDF provides constraints on models of chemical evolution. For example, the low mean metallicity of stars in the Galactic halo led Hartwick (1976) to conclude that the halo must have lost its gas, through outflows, before enrichment to higher metallicity could occur. On the other hand, the lack of metal poor stars in the solar neighborhood, relative to a Closed Box of chemical enrichment, is an evidence of gas inflow during chemical evolution (e.g., Pagel 1989). Additionally, the mean MDF may reveal radial or vertical gradients, possibly indicating viscous flows, the radial action of bars, or dissipational collapse.

As mentioned above, the fact that the bulge has a broad MDF was known for a long time. However only in the last ~ 15 years has the measured MDF been precise enough to allow some important conclusions on the bulge properties. Zoccali et al. (2008); Hill et al. (2011); Ness et al. (2013a); Rojas-Arriagada et al. (2014); Gonzalez et al. (2015) demonstrated that the bulge MDF is bimodal, with the two peaks having metallicity a few dex below and a few dex above solar, respectively. While the mean metallicity changes across the bulge area, the position of the two peaks does not, thus the mean metallicity gradient, also known for a long time from photometry or low resolution spectroscopy (e.g. Terndrup 1988; Minniti et al. 1995) is in fact due to a different relative fraction of the two metallicity components. None of the studies mentioned above observed stars at latitudes $|b| < 4^\circ$. Due to the higher extinction close to the plane, previous studies of metallicities in the inner bulge ($|b| < 4^\circ$) are either based on very low number statistics, i.e., one or two dozens stars (e.g., Rich et al. 2007, 2012; Schultheis et al. 2015), or on ~ 100 stars with poorer metallicities, compared with those presented here (Babusiaux et al. 2014).

Interestingly, the bulge metal-rich and metal-poor sub-populations have vertical scale heights reminiscent of the local thin and thick disks, respectively, and consistent with the $[\alpha/\text{Fe}]$ ratios of the thin and thick disks (Alves-Brito et al. 2010; Hill et al. 2011; Gonzalez et al. 2011b). However, these bulge sub-populations have ~ 0.4 dex higher $[\text{Fe}/\text{H}]$ than the average thin and thick disk stars in the solar neighborhood. Thus, if these bulge sub-populations really represent the inner thin and thick disks, a radial $[\text{Fe}/\text{H}]$ gradient near -0.05 dex/kpc is implied for both disks (McWilliam 2016). If the bulge was built by the growth and buckling of a stellar bar, then inner thin and thick disk stars entrained into the bulge must have retained vertical scale heights characteristic of their origin, and resulting in the present-day vertical metallicity gradient. The MDF and the chemical composition of bulge stars have been recently reviewed by Ness & Freeman (2016); McWilliam (2016).

Finally, an observational tool that can be critical to discriminate among different formation scenarios is the stellar kinematics. Indeed, galactic bars usually present streaming motions along the major axis, due to the elongated orbits that sustain the bar. For the same reason, the phase space of stars in the bar shows a significant vertex deviation, contrary to the stars in a spheroidal component, showing a more isotropic velocity distribution, with a higher dispersion. Although Saha & Gerhard (2013) demonstrated that a pre-existing spheroid would increase its rotation velocity if a bar is formed at later times, the other kinematical differences mentioned above help discriminate between two or more populations if they belong to different spatial structures. The interested reader may refer to the review on bulge kinematics by Babusiaux (2016). The most relevant, recent investigations demonstrated that the bulge shows cylindrical rotation (Howard et al. 2009; Ness et al. 2013b; Zoccali et al. 2014), with a velocity dispersion increasing towards the Galactic plane, including a peak in the inner ~ 2 degrees from the Galactic center (Zoccali et al. 2014, hereafter Paper I). The kinematical properties of the metal poor and metal rich bulge components are slightly different, with the metal poor having higher velocity dispersion, at least in the outer bulge (Ness et al. 2013b).

We present here the MDF derived for 26 bulge fields, observed within the GIRAFFE Inner Bulge Survey (GIBS), an ESO Large Programme (ID 187.B-0909; PI: Zoccali) carried out with the GIRAFFE spectrograph of the FLAMES instrument (Pasquini et al. 2002) at the Very Large Telescope (VLT). The aim of the survey is to investigate how the metallicity and radial velocity distributions vary across the bulge area, with special attention to the fields close to the Galactic plane, at $b = -2$ and $b = -1$, not explored by other surveys. We combine here the metallicities of the stars with their radial velocities, already discussed in Paper I, in order to characterize the spatial distribution and kinematics of the two bulge metallicity components.

2. The data

The present investigation is based on spectra for $\sim 5500^1$ RC stars in several fields across the Galactic bulge, as shown in Fig. 1. All of them are located within the region mapped by the VVV Survey ($-10 < l < +10$ and $-10 < b < +5$; Minniti et al. 2010).

The targets were selected from the near infrared CMDs obtained within the VVV Survey, and calibrated to the 2MASS photometric system as in Gonzalez et al. (2011c). The target selection, discussed in Paper I, is shown in Fig. 2: the GIRAFFE targets are RC stars, in a relatively narrow range of apparent magnitude around the RC peak. The size of the target box is allowed to vary in different fields, according to the stellar density of the field, and the number of targets observed, spanning on average $\Delta J_0 \approx 0.5$ mag, corresponding to about 1 kpc along the line of sight. In Fig. 2 the observed stars are color coded according to their metallicity (see caption), and a color histogram of the targets is compared with that of all the RC stars. This is meant to emphasize that our target selection does not impose any significant bias in metallicity, except excluding the most metal poor stars ($[\text{Fe}/\text{H}] \lesssim -1.5$) that, if older than 10 Gyr, would end up in the blue horizontal branch. The absence of a metallicity bias is

¹ The kinematical analysis presented in Paper I was based on ~ 6500 stars, because it included archive spectra for 5 extra fields at $b = -2^\circ$ (from Prog. ID 089.B-0830) and a different, larger sample at $(0, -6)$, from Vázquez et al. (2015). All these spectra had a lower S/N, good for radial velocity measurement, but not for reliable metallicity measurements.

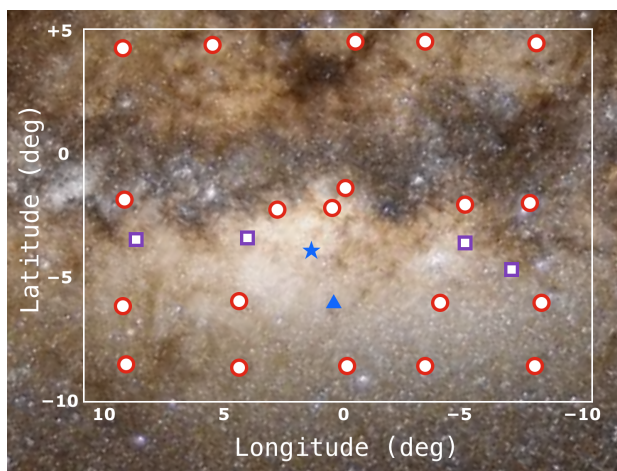


Fig. 1. Position in the sky of the 26 GIBS fields presented here. The large square is the area covered by the VVV Survey. Red circle are fields observed at low resolution (LR8), purple squares are field observed at high resolution (HR13 Gonzalez et al. 2015, ; Paper II). The blue star is the Baade's Window field used for the CaT calibration (Vásquez et al. 2015), and the blue triangle is the (0, -6) field discussed in Zoccali et al. (2008).

especially relevant in the interpretation of the MDFs for the two innermost field (one of which shown here) where we find a significant metal poor population.

Two independent sets of stars were observed within each field, for a total of ~ 210 stars. The two sets are identified as F1 and F2 in our tables. In a few fields that we considered particularly interesting, four sets of stars were observed instead, for a total of ~ 430 stars. Those fields are the two closest to the Galactic center, at (0, -1) and (0, -2), and the field at (0, -8) because it shows the double RC feature, signature of the presence of X-shape (or boxy/peanut shape) as demonstrated by McWilliam & Zoccali (2010); Nataf et al. (2010); Saito et al. (2011); Wegg & Gerhard (2013). In the (0, -8) field we observed two sets of stars in the bright RC (bRC-F1 and bRC-F2) and two sets in the faint RC (fRC-F1 and fRC-F2).

A detailed description of the target selection strategy, observations and the spectrum extraction and calibration is given in Paper I. Table 1 in that paper lists the coordinates of all the fields, together with the number of targets, the spectral setup, and the total exposure time associated to each of them. Here we recall that most of the GIBS fields were observed with the LR8 setup, covering the Calcium II triplet (CaT) feature (8206-9400 Å) at resolution $R = 6500$. Four fields at $b \sim -3.5^\circ$ were observed at higher resolution using setup HR13 (6120-6405 Å). Abundances for those are discussed in Gonzalez et al. (2015, ; hereafter Paper II).

Spectra for stars in two extra fields were added here to the original Large Programme. The first one consists in a sample of 178 RC stars in Baade's Window, at $(l, b) = (1, -4)$, marked as a star in Fig. 1. These stars, observed through setup HR13, were presented in Hill et al. (2011) but have been re-analyzed in Paper II, and we adopted here metallicities from the latter work. A subset (111) of these stars were also observed with setup LR8, and 80 of them were used to derive the CaT to [Fe/H] calibration, presented in Vásquez et al. (2015) and adopted here. The second additional dataset consists of 213 RGB stars in a field at $(l, b) = (0, -6)$ from Zoccali et al. (2008). Note that these stars are *not* the same as included in Paper I. Because it was focused on kinematics only, Paper I included a sample of 454

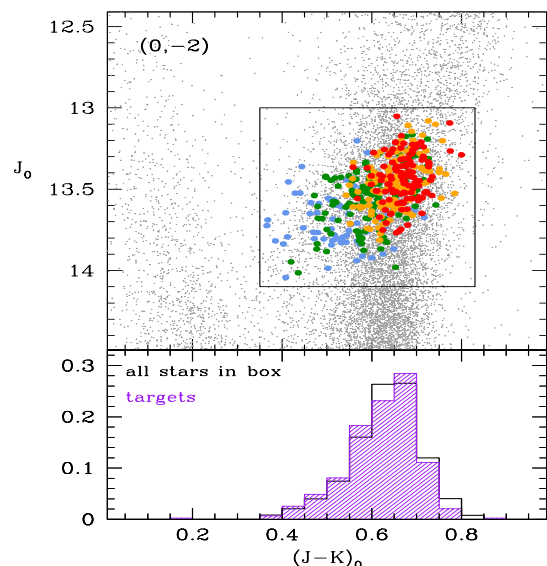


Fig. 2. Example of the GIBS target selection criteria for the LRP0m1 field. Top: the VVV CMD together with the 432 GIRAFFE targets, color coded according to their metallicity (blue: $[\text{Fe}/\text{H}] < -0.5$ dex; green: $-0.5 < [\text{Fe}/\text{H}] < -0.1$; orange: $-0.1 < [\text{Fe}/\text{H}] < +0.3$ and red: $[\text{Fe}/\text{H}] > +0.3$). Bottom: color histogram of all the stars in the FLAMES field, in the black box of the CMD, compared with the color histogram of the selected targets.

RC stars, at (0, -6), from Vásquez et al. (2013), that are more numerous than the sample analysed here. However, those spectra had lower S/N and, most importantly, the dispersion direction encompassed the four detectors of the IMACS@Magellan mosaic, preventing a reliable continuum definition and therefore hampering the metallicity determination. With the focus on the MDF, here we replaced the Vásquez dataset with the RGB stars from Zoccali et al. (2008). The latter, although smaller in number, have been observed with the same instrument as our HR sample. The analysis carried out in Zoccali et al. (2008) is compatible with the one in Paper II within 0.1 dex, as verified in the Baade's Window field. The targets at $(l, b) = (0, -6)$ are the only ones in the present work that lie on the RGB, slightly above the RC.

In summary, we discuss here the MDF for 26 fields, shown in Fig. 1. For 20 of them, shown as red circles, we have LR8 spectra with $R=6500$. Metallicities were derived by measuring CaT equivalent widths and converting them to [Fe/H] following the recipe in Vásquez et al. (2015). For 6 other fields (blue squares, star and triangle) we have spectra at $R=22,500$ and [Fe/H] measurements were derived from equivalent widths of isolated FeI lines, constraining also stellar surface parameters.

3. Iron abundances

3.1. High resolution spectra

The analysis of the high resolution spectra was presented in Paper II, where the details of the adopted method to obtain [Fe/H] and [Mg/Fe] can be found. Here we briefly recall how [Fe/H] abundances were derived.

Stellar atmospheric parameters were discussed in Paper II, namely effective temperature (T_{eff}), surface gravity ($\log g$), microturbulent velocity (ξ), and metallicity ([Fe/H]) using the standard iterative method based on the equivalent widths of isolated

FeI lines. Initial abundances are derived from each line by adopting first guess photometric temperature and gravity, and these are later refined by imposing excitation and ionization equilibrium. The code GALA (Mucciarelli et al. 2013) has been used here to perform this task automatically.

First guess photometric temperatures were calculated by applying the calibration by Ramírez & Meléndez (2005) to the $(V - K_s)$ magnitudes from OGLEII (Udalski et al. 2002) and the VVV catalogues in Gonzalez et al. (2012). The reddening maps in the latter paper were also used to correct for extinction. Absolute V-band magnitudes were derived using mean line-of-sight distances to each specific field from Gonzalez et al. (2013) and the bolometric corrections from Alonso et al. (1999). These are then used to estimate photometric gravities based on the classical formula:

$$\log(g) = \log(g_\odot) + \log\left(\frac{M_*}{M_\odot}\right) + 0.4(M_{\text{Bol},*} - M_{\text{Bol},\odot}) + 4\log\left(\frac{T_{\text{eff},*}}{T_{\text{eff},\odot}}\right)$$

where $M_{\text{Bol},\odot} = 4.72$, $T_{\text{eff},\odot} = 5770$ K, and $\log(g_\odot) = 4.44$ dex. As usual, we adopted a fixed value of $M_* = 0.8M_\odot$. Global metallicity and microturbulent velocity were fixed to 0.0 and 1.5, respectively, as a first step.

An initial ATLAS9 stellar model atmosphere was constructed using these first guess values. This was later updated by GALA while iteratively searching for spectroscopic effective temperatures and microturbulent velocity, by imposing excitation equilibrium and the null slope of iron abundance versus equivalent width of the Fe line, respectively. As discussed in Gonzalez et al. (2015), the mean uncertainty in the metallicity measurements is $\sigma_{[\text{Fe}/\text{H}]} = 0.2$ dex, reaching as low as 0.1 dex at the low metallicity end, and up to 0.4 dex at the high metallicity end.

The method described above has been used, identically, to derive the abundances for the four GIBS fields observed at high resolution (blue squares in Fig. 1) and for the Baade’s Window giants used by Vázquez et al. (2015) to derive the CaT to $[\text{Fe}/\text{H}]$ calibration. The latter is applied here to the low resolution spectra, thus insuring that the final metallicities adopted for our stars are all in the same scale.

3.2. Low resolution spectra

The pre-reduction of the LR8 spectra, together with the fitting of the three CaT lines is described extensively in (Vázquez et al. 2015) where the CaT versus $[\text{Fe}/\text{H}]$ calibration was derived. We summarize here the main steps. The spectra were de-biased, flat-fielded extracted and wave calibrated using the GIRAFFE pipeline (version 2.8) provided by ESO. Sky subtraction was instead applied with IRAF, by first combining the ~ 20 sky fibres in a master sky, which was then subtracted from the science spectra by means of the task `skytwake`. The spectra were then normalized with the IRAF task `continuum`, and finally cross-correlation (task `fxcor`) was performed against a template synthetic spectrum in order to bring the spectra to the restframe velocity.

Equivalent widths (EWs) of the two strongest CaT lines (8542 Å and 8662 Å) were measured by fitting the observed flux with the sum of a Gaussian component, fitting the line core, plus a Lorentzian function, fitting the wings. Vázquez et al. (2015) presented several tests of the stability of such fits against metallicity and signal to noise, by means of synthetic spectra. They demonstrated that the weakest CaT line at 8498 Å (hereafter

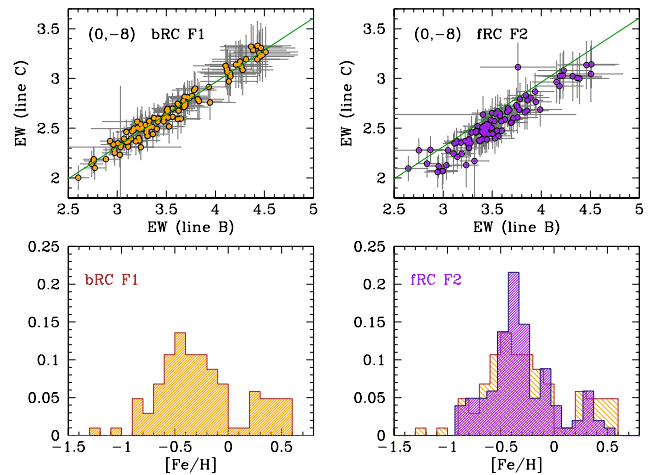


Fig. 3. Top panels: trend of the EW of line C versus line B, for two different fiber allocations in the field at (0, -8). The orange points are 103 targets in the bright RC, while the purple ones are 102 targets in the faint RC. The green line is the same trend for the RC stars in Baade’s Window used to derive the CaT vs $[\text{Fe}/\text{H}]$ calibration. While the orange targets beautifully follow the expected ratio, the purple points have an offset, that might be due either to an overestimation of line B and/or to an underestimation of line C. Bottom panels: (left) MDF derived from the 103 targets with good line ratio; (right) the MDF derived from the targets with offset line ratio, in purple, is compared with the orange one, obtained from targets with good line ratio.

line A), does not behave smoothly with metallicity, as the two stronger lines (B and C), and it is the most affected by sky subtraction, due to the presence of two sky lines close to its wings. For this reason the CaT-to- $[\text{Fe}/\text{H}]$ calibration presented in (Vázquez et al. 2015) relies only on the two stronger lines.

Figure 5 in Vázquez et al. (2015) demonstrates that, for the stars in Baade’s Window used to derive the CaT-to- $[\text{Fe}/\text{H}]$ calibration, the ratio between line C and line B is remarkably constant along metallicity. The ratio of these two lines was compared with that of Baade’s Window for the stars in all the fields analysed here. Most of the stars indeed follow the same line ratio as the calibrators in Baade’s Window. In some fields, however, all the stars observed within a given exposure show a shift in the ratio of lineC-to-lineB, with respect to Baade’s Window (Fig. 3). The shift is constant for all the stars, i.e., it does not depend on the metallicity nor the surface parameter of the individual stars. It is also independent from the radial velocity of each star, which differs by up to 400 km/s. We conclude that it must be due to an improper continuum normalization (i.e., a residual slope in the pseudo-continuum of the two lines). A variation of less than 1% in the EWs (upper right panel of Fig.3) corresponds to a shift in the pseudo-continuum very hard to detect. Despite our many attempts, it was impossible to relate the presence of the offset to any specific sky condition (Moon, humidity, etc...), nor to correct it. Fortunately, the impact of the offset on the final metallicity is very small, if any (lower right panel). We therefore did not correct for this effect, keeping in mind that it happens, with the same magnitude shown in Fig. 3, for 10 sets of stars, in 7 fields out of the 20 observed with the CaT setup².

In order to apply the CaT-to- $[\text{Fe}/\text{H}]$ calibration equation from (Vázquez et al. 2015) one needs to calculate the so-called *re-*

² The affected sets of stars are the following: LRp5p4-F1, LRp5p4-F2, LRp0m1-F3, LRp3m2-F2, LRp0m2-F2, LRp0m2-F3, LRM8m2-F2, LRp0m8-fRC-F2, LRM3m8-F2, LRM8m8-F2.

duced EW parameter, W' , defined as

$$W' = \Sigma EW + 0.384(K - K_{RC})$$

where ΣEW is the sum of the EWs of line B and line C, and the term $0.384(K - K_{RC})$, is a correction that takes into account simultaneously the effect of the surface gravity and temperature of the star, parametrized as the magnitude difference between the star and the RC, in that specific field.

To that end, the observed K_s magnitudes of all stars were corrected using the interstellar extinction maps of (Gonzalez et al. 2012) before calculating the difference with respect to peak dereddened RC magnitude in that field. Since the stars were chosen to be on the RC, this difference is very close to zero for all our targets. We nevertheless included this correction, because the target selection was done on the observed magnitudes, before the extinction map was published. Therefore, in the innermost, most extincted fields, some stars might end up slightly displaced from the peak RC in the de-reddened CMD. The CaT calibration presented in Vázquez et al. (2015) has a rms uncertainty of 0.2 dex.

The coordinates, magnitudes, metallicities and radial velocities of the GIBS targets discussed here are given in the electronic version of Table 1.

4. The bulge Metallicity Distribution Function

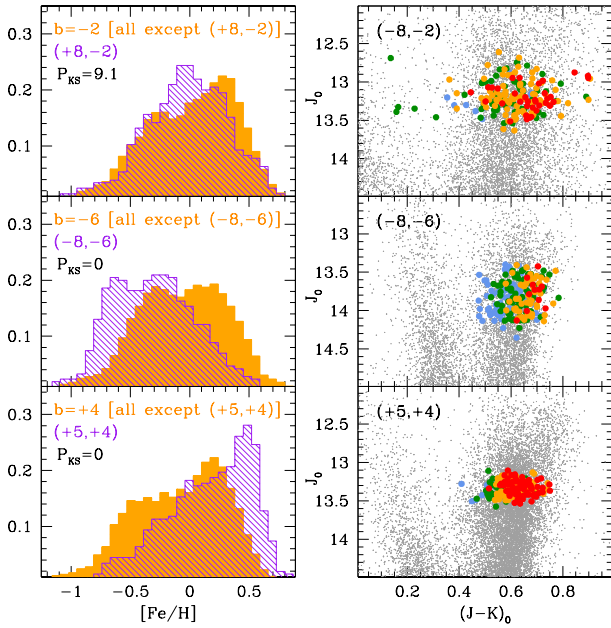


Fig. 5. Left panels: MDF of the discrepant fields, compared with the global MDF of the other fields at the same latitude. The p-value of the Kolmogorov-Smirnov test comparing these peculiar MDFs to the global MDF is indicated. Right panels: corresponding target selection for these fields. Targets are color-coded according to their metallicity, with blue dots having $[\text{Fe}/\text{H}] < -0.5$ dex, green $-0.5 < [\text{Fe}/\text{H}] < -0.1$, orange $-0.1 < [\text{Fe}/\text{H}] < +0.3$ and red $[\text{Fe}/\text{H}] > +0.3$.

The resulting metallicity (iron) distribution function for the 26 fields is shown in Fig. 4. Panels in this figure are arranged in the same way as the fields in Fig. 1, with labels within each panel showing the galactic coordinates of each field, and the number of stars included in the histogram. The orange histograms refer

to the fields observed at low resolution (Sec. 3.2), the green histograms are the fields observed at high resolution (Sec. 3.1) with our ESO Large Programme, and the blue histogram are the 213 RGB stars from Zoccali et al. (2008) at (0,-6), and the 178 RC stars from Hill et al. (2011) in Baade's Window.

All the histograms presented in this Section have been obtained as Average Shifted Histograms. Specifically, three histograms were constructed, each with a bin of 0.21 dex and starting points at $[\text{Fe}/\text{H}] = -2.0, -1.93$ and -1.86 (i.e., shifted by 0.07 dex), respectively. A vertical line, fixed at $[\text{Fe}/\text{H}] = 0$, has been drawn in each panel, as a guide to the eye. All the fields in Fig. 4 show a clear bimodality, except for two of them (LRp8m2, LRM8m6) that look unimodal. In order to assess the significance of the bimodality, we have run a Gaussian Mixture Model (GMM Muratov & Gnedin 2010) allowing for the presence of one, two, or three Gaussians with different mean and dispersion. The best fitting solution, for most of the fields, is the trivariate one, with a tiny peak for $[\text{Fe}/\text{H}] < -0.8$. This peak is usually made up of a handful of stars, and in some fields is so small that it is not even visible in Fig. 4. Suppressing this peak, and fitting only two Gaussians, however, resulted the metal poor Gaussian being very broad, enough to include these few stars, and therefore extending to supersolar metallicities. This peak would unrealistically include some of the most metal rich stars of the sample. The triple Gaussian fit did not converge in four fields (LRp5p4, LRM5m2, HRp8m3, Baade's Window); for these fields the data were best fit with double Gaussians.

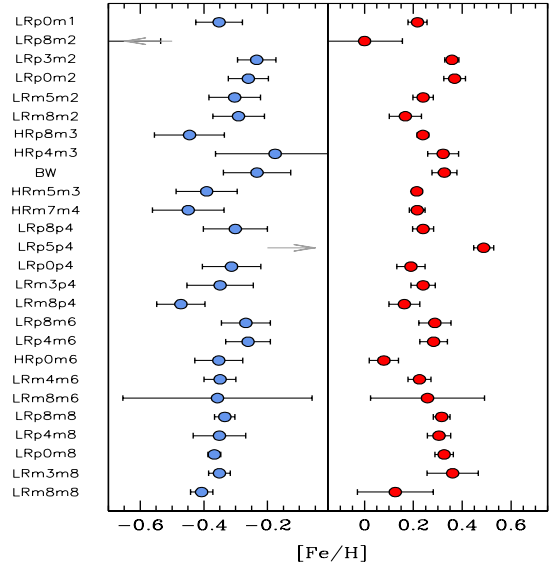


Fig. 6. Peak metallicity of the metal poor (blue) and metal rich (red) Gaussians fitted in Fig. 4. The name of the fields are listed on the left, from the closest to the plane at the top, to the ones in the outer bulge at the bottom.

In fields LRp8m2 and LRM8m6 the two Gaussian model did not yield a significantly better fit compared to a single Gaussian. It would seem unrealistic that the bulge contains two metallicity components, with a separation of ~ 0.6 dex in $[\text{Fe}/\text{H}]$, *except* in these two fields. We therefore double checked the target selection and the velocity distributions of stars in these two fields, to ensure that we are sampling the same populations as in the others. From Fig. 10 below, we see that at (+8, -2) and (-8, -6), the velocity versus metallicity scatter plots do not show any strange feature, that could indicate a possible sub-population.

Table 1. Coordinates, VVV magnitudes, radial velocities and metallicities of the program stars.

ID	RA (J2000)	DEC (J2000)	J	K_s	RV	Err RV	[Fe/H]
LRp0m1_F1_OGLE5_140424	17:50:20.66	-29:58:42.30	14.617	13.234	-42.9	2.1	-0.33
LRp0m1_F1_OGLE5_141397	17:50:19.03	-29:58:04.10	14.761	13.361	198.0	2.3	-0.65
LRp0m1_F1_OGLE5_145942	17:50:19.62	-29:56:20.40	14.166	12.551	253.0	2.4	-0.10
...

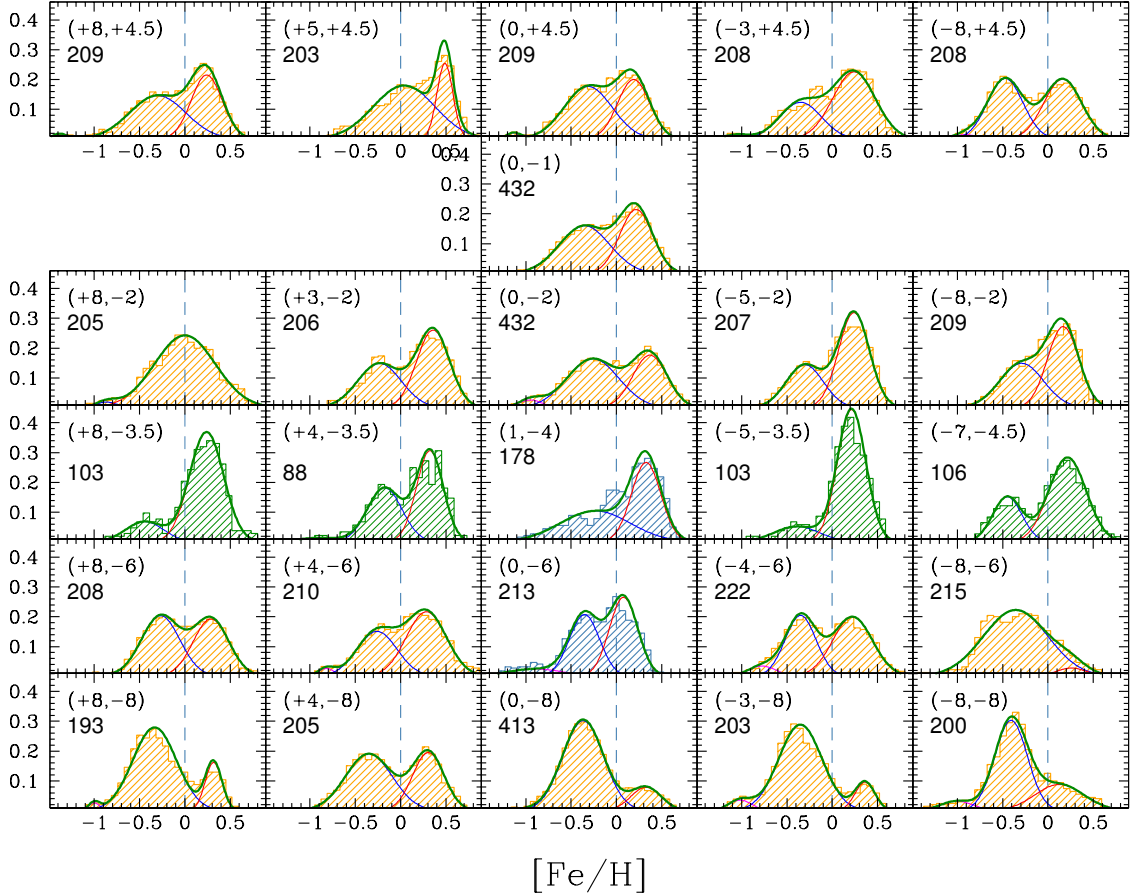
**Fig. 4.** Metallicity distribution function (MDF) for the 26 fields of the present study. Orange histograms have been derived from CaT spectra, while green histograms come from the high resolution spectra discussed in Paper II. Blue histograms are from our previous works. Panels are arranged like the fields in the sky, with approximate coordinates indicated in the labels. The number of stars observed in each field is also labelled for each field.

Fig. 5 (left panels) shows the p-value of Kolmogorov-Smirnov test comparing the MDF of these fields to the global MDF for the other fields at the same latitude. In the case of the (+8, -2) field, the p-value (9%) does not permit rejection of the hypothesis that this field is drawn from the same MDF. The top right panel shows the target selection for this field: while the selection was done on the observed CMD (before the VVV reddening maps were available), de-reddened magnitudes are shown here; therefore, the targets are no longer confined to a CMD box. This field in particular is very close to the plane, where differential reddening is non negligible. After correction, some targets seem to belong to the foreground disk rather than to the bulge. Targets here are color coded according to their metallicity: blue points are stars with $[\text{Fe}/\text{H}] < -0.6$ dex, green with $-0.6 < [\text{Fe}/\text{H}] < -0.1$ dex, orange with $-0.1 < [\text{Fe}/\text{H}] < +0.3$ dex, and red with $[\text{Fe}/\text{H}] > +0.3$ dex. Contaminating disk stars all belong to the peak at $[\text{Fe}/\text{H}] \sim -0.2$ dex. Indeed, removing stars

with color $(J - K)_0 < -0.35$ would change the p-value to 15%. We conclude that this field happened to have a larger disk contamination, due to the higher differential reddening. Its distribution is anyway compatible, within the statistical fluctuations of the present sample, with the global one at this latitude. Note also that the metallicity derived for disk stars would not be accurate, since their gravity differ significantly from that of CaT calibrating stars.

Stars in the field at (-8, -6) are shown in the middle panels. Here the MDF is much more metal poor than the global one, with null probability (10^{-11}) of having been drawn from it. On the other hand, the CMD does not show obvious contaminations, and neither does the velocity versus metallicity plot in Fig. 10. We do not have a plausible explanation for the observed difference between the MDF of this field and the global one at this latitude. Even if a unimodal Gaussian distribution would fit the MDFs of these two fields marginally better than a bimodal one,

we imposed a bimodal fit for consistency with the other fields. Obviously the position of the peaks will not be well constrained in this case.

Finally, another rather peculiar field is the one at $(+5, +4)$. In this case the MDF has two main peaks like all the others, but it is all shifted to metal rich values. Again, the target selection does not seem to be different from that of the other fields. This is one of the fields where the ratio of line B to line C has an offset with respect to the calibrating stars in Baade's Window. We have shown in Fig. 3 that the impact of this offset on the MDF is negligible, but in this field we have an offset in both target datasets (LRp5p4-F1 and LRp5p4-F2) hence we cannot really verify that. We will treat this field like the others, keeping in mind its peculiarity and ensuring that none of the conclusions drawn in the present paper is based on any of the fields in Fig. 5. Rather, we will be able to draw robust results *in spite of* the peculiar shape of the MDF in those fields.

In what follows we will try to characterize the two metallicity populations that we see in the bulge. We will assume that the tiny peak at $[\text{Fe}/\text{H}] \sim -1$ is made up by contaminating halo stars. Notice that our MDFs do not include very metal poor stars because our target selection criterion excludes stars outside the color range of the RC. Stars with $[\text{Fe}/\text{H}] < -1$, if they are old enough, would end up to the blue of the RC, and would therefore fall outside the target selection box. The MDFs for the fields at $|b| > 3^\circ$ confirm previous findings by our group (Zoccali et al. 2008), the ARGOS survey (Ness et al. 2013a) and the Gaia-ESO survey (Rojas-Arriagada et al. 2014). Namely, that the bulge has two metallicity components: with the metal poor one dominating at high latitude, and the metal rich dominating closer to the plane. The mean metallicity, therefore, has a gradient which is due to the different mix of the two populations, and it is mostly vertical, rather than radial (Paper II). Fig. 6 shows the metallicity of the metal poor (blue) and metal rich (red) peaks as fitted above. Errorbars were calculated by means of a non-parametric bootstrap (drawing from the input sample with repetitions) of 100 realizations (Muratov & Gnedin 2010). Overall, the metal poor and metal rich peaks stay constant, within the errors, with only two fields rather discrepant, both of them discussed above.

The most important result from the present data is that, at latitude smaller than $|b| = 3^\circ$, the metal poor component becomes important again. Because the variation of the MDF with longitude, at constant latitude, is smaller than the variation as a function of height from the plane, we have coadded the stars in all the fields at constant latitude, and show the results in Fig. 7. Thanks to the larger statistics, the MDFs here are much smoother and the two Gaussian fits to stars with $[\text{Fe}/\text{H}] > -0.8$, obtained with the GMM, are excellent. The label in each panel states the fraction of metal poor stars, i.e., the relative contribution of the blue Gaussian to the total bimodal fit. This fraction is 0.77 at $b = -8.5^\circ$, drops continuously when moving closer to the plane, reaching a minimum of 0.29 at $b = -3.5^\circ$, and then goes back up to 0.6 at $b = -2^\circ$ and 0.53 at $b = -1^\circ$.

The MDF for the innermost ~ 2 degree from the Galactic center was derived by Rich et al. (2007) and Rich et al. (2012). They analysed near IR, high resolution spectra for ~ 15 M giants in each of two fields at $(0, -1)$ and $(0, -1.75)$, respectively, and found only metal rich stars, with only a few of them having $[\text{Fe}/\text{H}] < -0.3$, and none with $[\text{Fe}/\text{H}] < -0.5$. Babusiaux et al. (2014), on the other hand, derived the MDF from CaT spectra for 107 giants in a field at $(0, +1)$. They do find a metal poor population, rather similar to the present one at $(0, -1)$, although with a longer metal poor tail, possibly due to the slightly different target selection box. Finally, the presence of a metal poor

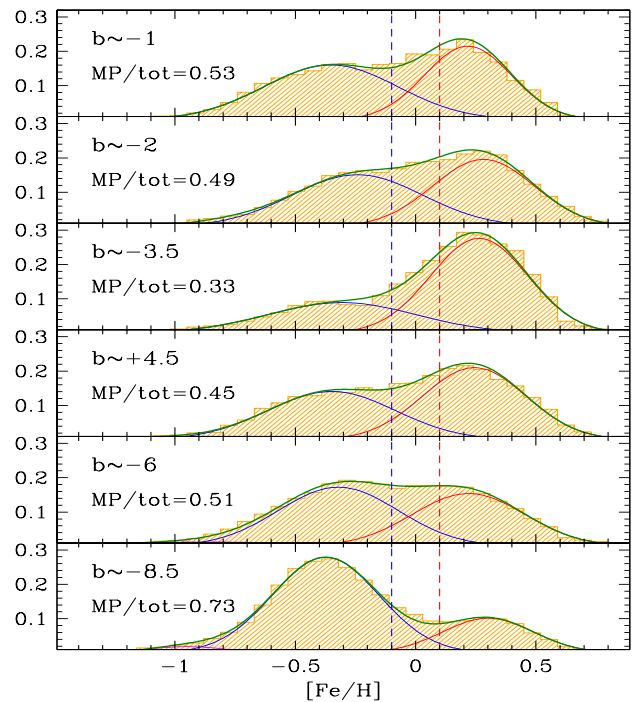


Fig. 7. MDFs of all the stars at constant latitudes, where fields at different longitudes have been combined. The fraction of metal poor stars, compared to the total, is listed in each panel. As discussed in the text, the fraction of metal poor stars decreases from $b = -8.5$ to $b = -3.5$, where it reaches a minimum, but then it rises again at latitude closer to the Galactic plane. The vertical dashed lines mark the limits of the metal poor and metal rich populations (see text).

component within a radius of 1 degree around the Galactic center was detected by Schultheis et al. (2015), from a sample of 33 M giants observed within the APOGEE data.

Two things are very clear from Fig. 4 and Fig. 7: *i*) the bulge does have two metallicity components; and *ii*) the spatial distribution of the components is different. In order to investigate the density distribution of the two components we need to convolve the information given in Fig. 4 with what we know about the bulge global density distribution. In other words, although the metal poor component is dominant in the outer bulge (at $b = -8.5^\circ$) it might not be very conspicuous, just because the stellar density at these latitudes is rather low. We investigate this specific point in the next Section.

5. Characterizing the two metallicity populations in the bulge

In this Section we will try to characterize the spatial distribution of the metal poor and metal rich stars, separately. We will also investigate the radial velocity distribution of the two populations. Let us stress, that although it will be clear that these two populations have different properties, this does not necessarily imply that they had different origin. Certainly, the difference in spatial and kinematical properties between the two metallicity components must be taken into account when studying bulge formation models which should ultimately provide the link to the physical processes behind them. The purpose of this paper, however, is to present and describe the observational data only.

5.1. Density distribution of red clump stars

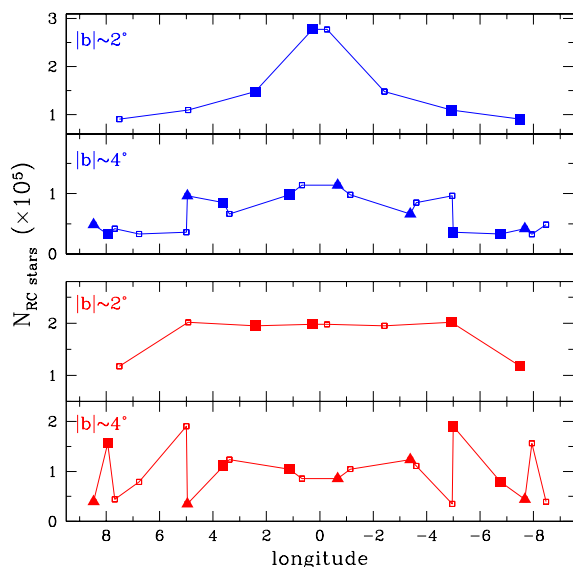


Fig. 8. Stellar density of RC stars, assumed to trace the global stellar density, for the metal poor (top panels, blue) and the metal rich (bottom panels, red) components. Filled squares/triangles refer to actual fields at negative/positive latitude, respectively. Open symbols are their mirror positions, when folded in longitude. Two strips at almost constant latitude are shown here, as indicated in the labels. Notice that the metal poor component has a steeper gradient towards the center, while the metal rich one has a very mild, if any, gradient at these latitudes.

Using the fact that the bulge MDF can be parametrised by two Gaussian components, each having a coherent spatial variation, the fraction of metal poor to metal rich stars given by the MDF in each field can be translated to a stellar density of each component individually. This can be done by using the bulge stellar density map from Valenti et al. (2016), who counted the number of RC stars across the bulge using PSF photometry from the VVV survey. We use this number and the relative fraction of metal-poor and metal-rich Gaussian components of each of the GIBS fields to calculate the corresponding number of metal poor and metal rich RC stars, in each field. The number of RC stars for each component of all fields is listed in Table 3.

In order to visualize the differences in the spatial distribution of metal poor and metal rich RC stars, Table 3 should be used to construct spatial density maps for the two components. This is challenging with the current data, because the GIBS field grid is relatively coarse. In order to improve the spatial resolution, we folded the field grid both in Galactic longitude and latitude. When doing so, we are imposing that the density maps must be symmetric both about l and b . While symmetry about the Galactic plane is very plausible, the orientation angle of the Galactic bar does produce an asymmetry in the projected density between positive and negative longitudes (Alard 2001; Valenti et al. 2016). For the present investigation, however, we are assuming that our data are not dense enough to allow us to detect differences between the near and far sides of the bar.

Figure 8 shows the number of RC stars in two strips at approximately constant latitude, as a function of longitude, for the metal poor (top panels, in blue) and the metal rich (bottom panels, in red) components. Filled symbols show the actual positions of the GIBS fields, at negative (squares) and positive (triangles) latitude. Open symbols are the mirror positions of these fields,

when folded in longitude. The two discrepant fields LRp8m2 and LRM8m6 have been omitted in this analysis. Figure 8 shows that the metal poor component is peaked towards the center, while the metal rich one has a fairly constant density distribution, at least at these latitudes. The rather flat distribution of metal rich stars resemble the RC surface density in Nataf et al. (2015, their Fig.13), at $|b|=5.5$, although the latter study included all the RC stars, without distinction on metallicity. Figure 8 shows a sub-sample of the real data, without any modeling nor fitting. It has however one important limitation, because the fields shown here have only *approximately* constant latitude: the fields at $|b| \sim 4^\circ$ actually span a range from $|b| = 3.5^\circ$ to $|b| = 4.5^\circ$. Other fields not shown here are even more scattered at different coordinates. A deeper analysis of what the data show, therefore, requires an interpolation and a two dimensional visualization.

We applied a bivariate linear interpolation to the irregular grid of GIBS fields using the *akima* package in R (Akima 1978) to produce stellar density maps of the metal poor and the metal rich components, as shown in Fig. 9. To construct the maps, we normalised the number of RC stars of each component by the maximum number of metal-poor RC stars so that the color code of the maps can be compared directly. We focus on the general shape of the maps instead of the details as the latter are highly dependent on the interpolation method and the non-uniform grid. For this reason, we smoothed the map using an isotropic Gaussian kernel with standard deviation of 1 deg. The fields LRp8m2 and LRM8m6 have been omitted from the maps because the fraction of metal poor to metal rich component obtained from them are not reliable in our opinion. In any case, thanks to the four fold symmetry that we chose to impose, the maps obtained with these fields included are only barely distinguishable from the ones presented here.

It is clear from Figure 9 that the density map of metal-poor RC stars is more concentrated than that of the metal-rich RC stars. Furthermore, the metal-rich map appears more elongated, or boxy, along Galactic longitude because of a steep drop in the stellar counts after $|b|=5$ at all Galactic longitudes. On the other hand, towards the central region of the maps, the metal-poor stars are not only seen to be more centrally concentrated but they also overcome the number of metal-rich RC stars.

5.2. Kinematics versus Metallicity trends

We present here a kinematical characterization of the sample stars, with particular emphasis on possible differences between the metal poor and metal rich components. Only the radial velocities, and velocity dispersions, available from the GIBS spectra are discussed here. The proper motions for the spectroscopic targets are currently under analysis from VVV data. They will allow us to calculate three-dimensional space velocities, which will be discussed in a forthcoming paper.

Figure 10 shows the galactocentric radial velocity of the sample stars versus their $[\text{Fe}/\text{H}]$, for all the fields. Orange points are the fields observed with the LR8 setup, in the CaT spectral region. Light blue points are the targets observed at higher spectral resolution. Green and pink points in the field at $(0, -8.5)$, refer to stars in the bright and faint RC, respectively, which were also observed with the LR8 setup. This figure shows that the distributions are fairly homogeneous. Although there are a few outliers with respect to the main radial velocity distribution, there are no obvious bimodalities, nor tight clumps suggestive of possible streams. Due to the bulge rotation, stars in the fields at positive longitudes (panels on the left side of this figure) have positive

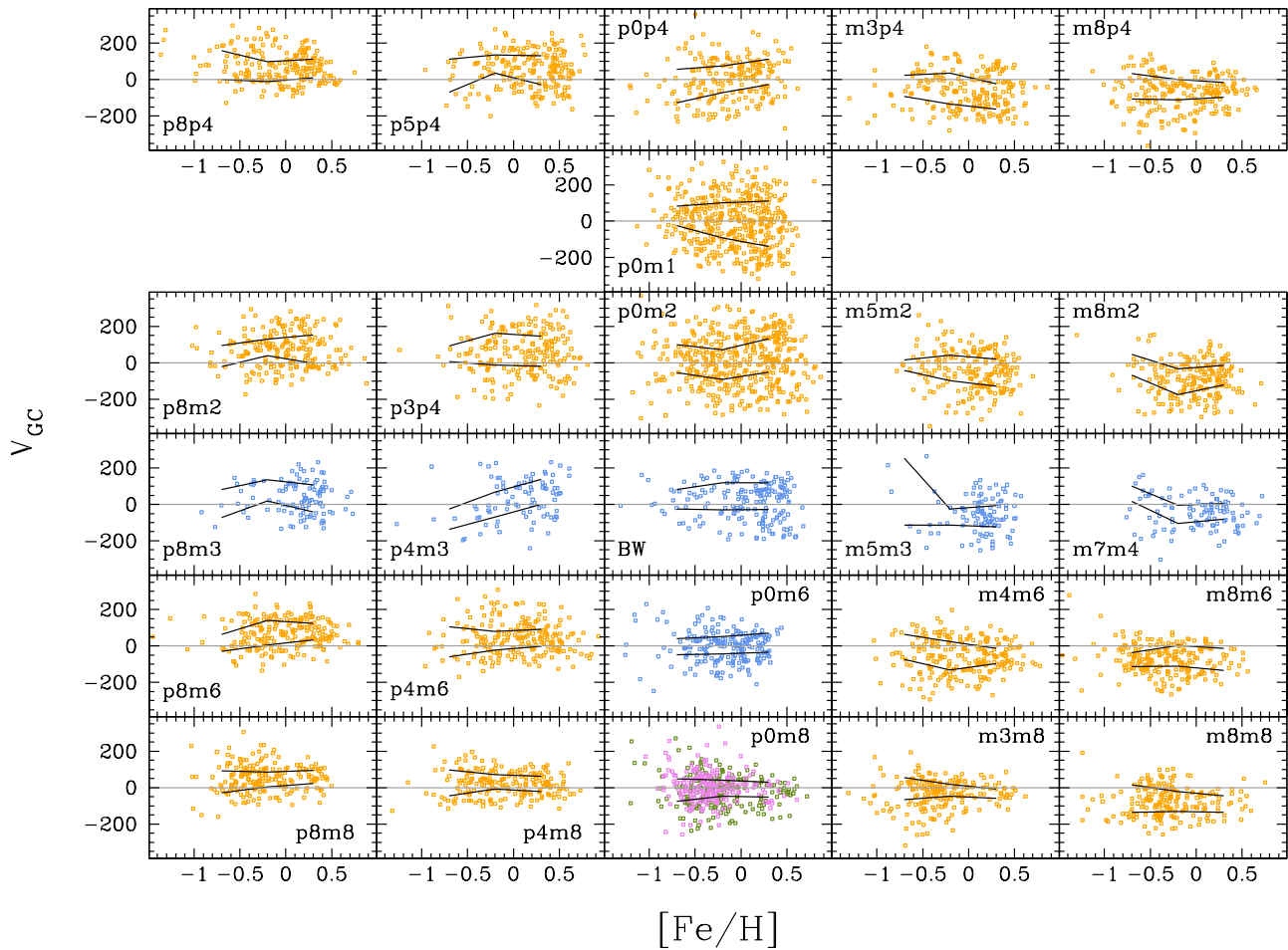


Fig. 10. Metallicity versus galactocentric radial velocity for all the targets in the GIBS fields. Orange points are stars observed in CaT, azure points are stars observed at high resolution. The field at $(0, -8)$ has a double RC: bright-RC targets are shown in green while faint-RC ones are shown in pink. The solid lines mark the $\pm 1\sigma$ interval around the mean velocity, at three different metallicities. See text for details.

(receding) mean velocities, while stars in fields at negative longitudes have negative (approaching) mean velocities.

This figure does not show any obvious trend of the mean radial velocity versus metallicity. It does show, however, that the velocity dispersion has a trend as a function of metallicity. Comparing, for example, the innermost field (second row from the top) with the outer one along the minor axis (pink and green points) the velocity dispersion of the metal poor stars, smaller than that of the metal rich stars in the innermost field, becomes larger in the outer field. This change is more evident along the minor axis, but is roughly conserved at $l \neq 0$. The black broken lines within each panel show the $\pm 1\sigma$ interval around the median, as a function of metallicity, for three 0.5 dex bins centered at $[Fe/H] = -0.7, -0.2$, and $+0.3$, respectively, with the aim of emphasizing the change of behaviour. As expected, the stars observed at high resolution at $b \sim -3.5$ (light blue points) show a very noisy behaviour, when binned in metallicity, because they are fewer in number, and also because at this latitude the metal poor component is very small compared to the metal rich one.

The variation of the velocity dispersion discussed above is best illustrated in Fig. 11 and Fig. 12, showing the velocity dispersion as a function of longitude, for different latitude, splitting the sample in a metal poor and a metal rich one. With the aim of separating the two components we have decided to make a

constant cut at $[Fe/H] = 0.0$, with the metal poor sample composed by stars with $[Fe/H] < -0.1$ dex, while the metal rich only contains stars with $[Fe/H] > +0.1$ dex. The narrow strip at $-0.1 < [Fe/H] < +0.1$ has been left out as a *no man's land*, because the large cross contamination would add more noise than number statistics. We have shown in Fig. 6 that the peaks do not move significantly from one field to the other, hence the choice of a constant cut (e.g., Fig. 7). The GMM yields the membership probability of each star to either population. However, in the overlap region, no model can possibly establish the membership probability on a one by one star basis. Therefore, we rather exclude the region where the overlap between the metallicity distribution is significant.

Figure 11 confirms what was already shown in the ARGOS data (Ness et al. 2013a), i.e., that the sigma of metal poor stars is on average higher than that of metal rich stars, at least for $|b| > 4^\circ$. It should be noted that the agreement with previous results should be taken qualitatively, because the metallicity cut in different studies has been chosen differently. In addition, the target selection in the ARGOS survey is such that many more metal poor (halo) stars are included. GIBS data allows us to extend the investigation to inner regions, showing that the trend of sigma versus metallicity is inverted at $b = -1^\circ$, at least along the bulge minor axis. Figure 12 best illustrates this point. It shows that for

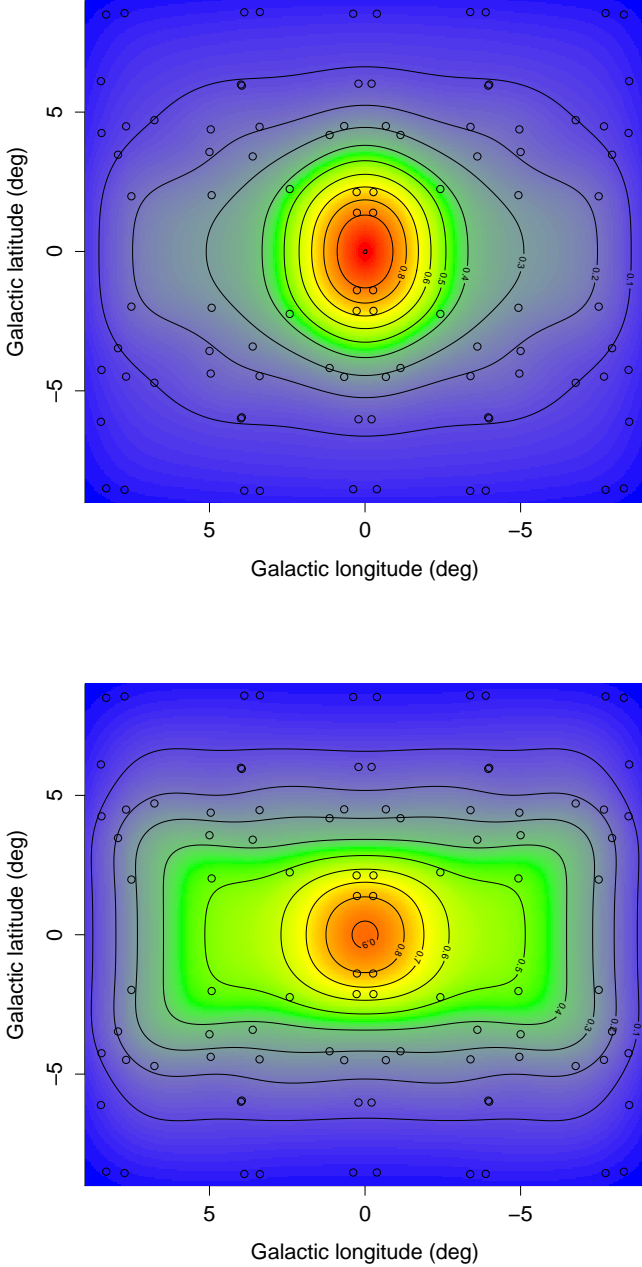


Fig. 9. Density map of metal-poor (top) and metal-rich (bottom) RC stars obtained using the two component MDF in each field and the total number of RC stars from Valenti et al. (2016). Open circles show the grid of fields used in the interpolation, resulting from folding the original map of GIBS fields with respect to both Galactic latitude and longitude. The number of RC stars of each component were normalised by the maximum of number of RC stars in the metal-poor map so they are color-coded to the same scale between values of 0 and 1. Contours are overplotted in both maps and correspond to differences of 0.1 in the normalised RC star counts.

$|b| > 3^\circ$ the metal poor component has a higher sigma compared to the metal rich one, with the difference becoming larger moving outward. At latitude $b = -2^\circ$ the two metallicity components have comparable sigma, while at $b = -1^\circ$ it is the metal rich component that shows a higher sigma. Unfortunately we only have one field at this latitude, but there are 432 targets in it, and

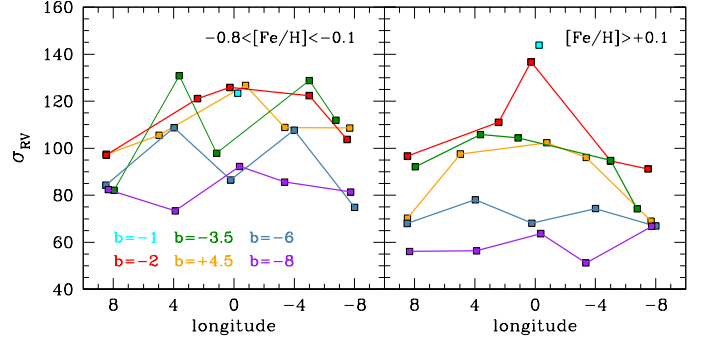


Fig. 11. Velocity dispersion as a function of longitude, for fixed latitudes shown in different colors. Metal poor stars are shown in the left panel, metal rich ones in the right panel.

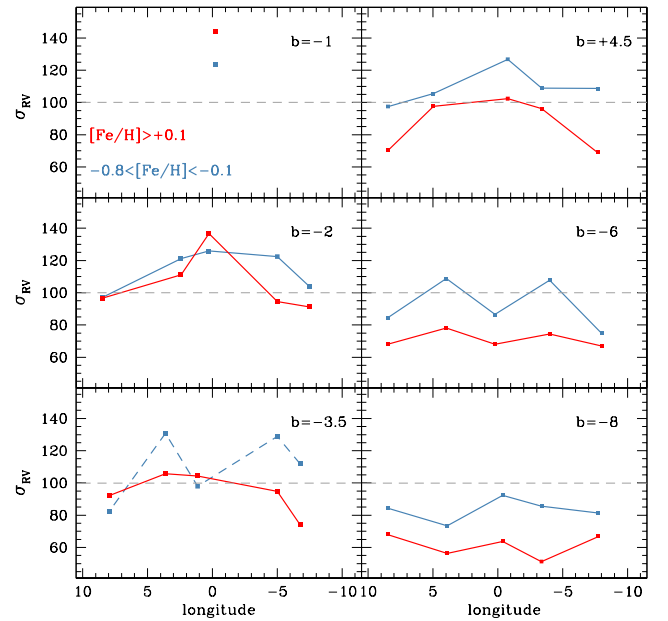
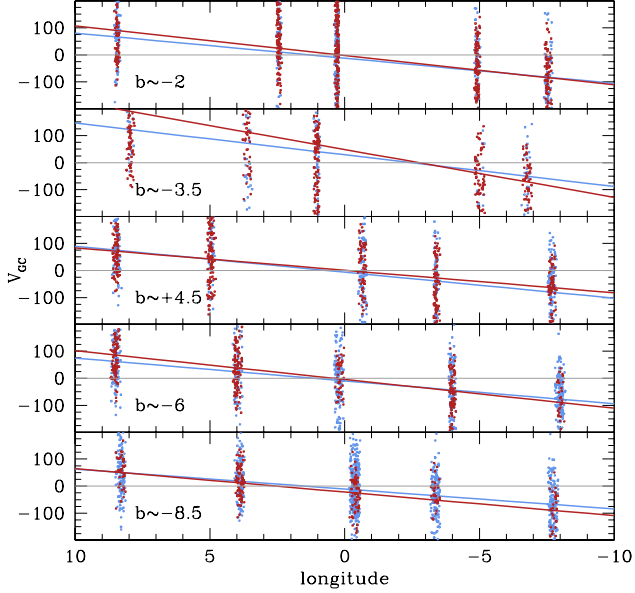


Fig. 12. The trend of velocity dispersion with longitude, in 6 strips of constant latitude. The horizontal dashed line at $\sigma_{RV}=100$ has been drawn to guide the eye. Notice that metal poor component has a higher velocity dispersion, compared to the metal rich one, in the outer bulge $b > 3.5$. However at $b = -2$ σ_{RV} is roughly equal for both metallicity bins, while at $b = -1$ the σ_{RV} for the metal poor sample lies below that of the metal rich population. Notice that the metal poor component at $b = -3.5$ contains very few stars, for this reason the trend is noisy, it is shown with a dashed line.

therefore the velocity dispersion measurement is robust. An indication of the inversion in the sigma versus metallicity trend, at very low latitudes, was already found in the data by Babusiaux et al. (2014), (see also Babusiaux 2016). With its very homogeneous target selection, the GIBS survey allows us to confirm that the inversion is real. This observational result seems to be due to the fact that the dispersion of the metal poor stars increases from the outer bulge ($b = 8^\circ$) towards the plane, although slower than that of metal rich stars, but then it stays constant in the three strips at $b = -3.5^\circ, -2^\circ, -1^\circ$. In other words, the velocity dispersion of the metal rich component has a gradient with latitude much stronger than that of the metal poor component.

Table 2. Slope of V_{GC} vs longitude, in 5 latitude strips.

Latitude	[Fe/H]<-0.3	[Fe/H]<-0.1	[Fe/H]>+0.1	[Fe/H]>+0.2
$b \sim -2^\circ$	8.2 ± 1.4	9.3 ± 1.1	10.9 ± 1.0	10.8 ± 1.1
$b \sim -3.5^\circ$	12.4 ± 3.2	11.7 ± 2.6	17.7 ± 1.2	19.1 ± 1.5
$b \sim -4.5^\circ$	8.6 ± 1.3	9.6 ± 1.1	8.3 ± 1.0	9.2 ± 1.1
$b \sim -6^\circ$	7.8 ± 1.0	8.4 ± 0.8	10.6 ± 1.0	10.8 ± 1.1
$b \sim -8.5^\circ$	7.0 ± 0.7	7.4 ± 0.6	8.7 ± 0.8	8.3 ± 0.8

**Fig. 13.** Galactocentric radial velocity versus longitude, at \sim fixed latitudes, as indicated in the labels. Metal poor stars ($[Fe/H] < -0.1$) are shown in blue, metal rich stars ($[Fe/H] > +0.1$) in red. A linear relation has been fit in each panel, separately for each metallicity component. Metal poor stars rotate marginally slower than metal rich ones.

Kunder et al. (2015) recently suggested that bulge RR Lyrae, tracing the oldest, more metal-poor component, rotate slower than RGB and RC stars. We investigate whether this signature is imprinted in the present data as well. Figure 13 shows the galactocentric radial velocity for all the stars, as a function of longitude, at fixed latitudes. Metal poor stars ($[Fe/H] < -0.1$) are shown in blue, metal rich stars ($[Fe/H] > +0.1$) in red. A linear relation, including the errors in radial velocity, was fit to the data in each panel, for the two metallicity components individually. Metal poor stars show a marginally slower rotation, i.e., a flatter slope. Adopting the metallicity cuts mentioned above, and used elsewhere in this paper, the slopes are always compatible within the errors. However if we move the metal poor cut at -0.3 dex, and the metal rich one at $+0.2$, i.e., we exclude a larger metallicity bin, as cross-contaminated, then the difference between the two slopes become more significant (Table 2). In other words, although the signal is marginally significant in these data, the GIBS sample confirms the findings by Kunder et al. (2015), that metal rich stars rotate faster than metal poor ones.

6. Conclusions

We presented the metallicity of ~ 5500 RC stars in 26 fields across the Galactic bulge. In all but two fields, the metallicity distribution is clearly bimodal with a metal poor component centered at $[Fe/H]_{MP} \approx -0.4$ dex and a metal rich component centered at $[Fe/H]_{MR} \approx +0.3$ dex. A small (few %) population of

stars with $[Fe/H] < -0.8$ is also identified in most of the fields, tentatively interpreted as halo contamination. The latter population is highly incomplete, because our target selection box does not extend to the blue of the RC, therefore we did not attempt to characterize it.

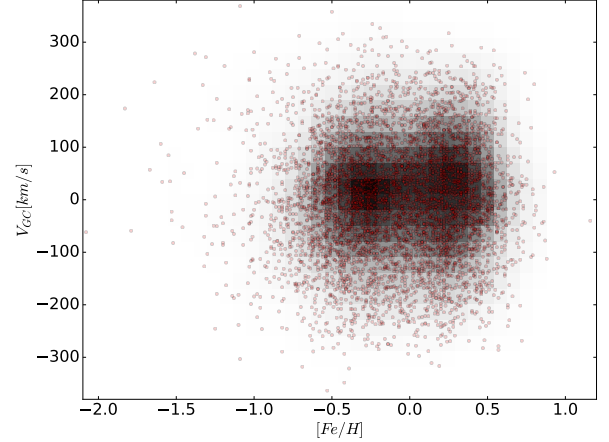
**Fig. 14.** Metallicity versus galactocentric radial velocity for the whole sample discussed here. The two metallicity components, that we call metal rich and metal poor, respectively, are clearly seen here.

Figure 14 shows the metallicity versus galactocentric radial velocity for all the stars in the present sample. Two populations in metallicity are clearly seen here. No stars were measured outside this figure's box, i.e., we do not detect high velocity stars, inconsistent with the tail of the main velocity distribution. The two main bulge components peak roughly at the same metallicity in different fields, but the relative fraction of stars in each of them changes dramatically across the bulge area, giving rise to well known radial gradients in the bulge mean metallicity. In the outer region studied here ($b = -8.5^\circ$), the metal poor component largely outnumbers the metal rich one, with the former accounting to 73% of the total number of targets observed at this latitude, and the latter to the remaining 27%. The relative fraction of metal poor stars drops to 33% of the total at $b = -3.5^\circ$: a result in very good agreement with previous findings by the ARGOS (Ness et al. 2013a) and the Gaia-ESO (Rojas-Arriagada et al. 2014) surveys.

The present dataset allows us to reach latitudes closer to the Galactic plane than previous studies, probing the population of the inner bulge. A first, important result of the present work is that the relative fraction of metal poor stars increases again from $b = -3.5^\circ$ to $b = -2^\circ$ and $b = -1^\circ$, reaching 49% and 53% of the total in the latter two fields, respectively.

Having demonstrated that the bulge includes two metallicity components whose relative fraction changes across the bulge area, i.e., they have a different spatial distribution, we mapped their density distribution by coupling the relative fractions estimated here with the bulge stellar density map derived in Valenti et al. (2016). The resulting density maps, shown in Fig. 9, demonstrate that the metal poor component has a spheroid-like spatial distribution, versus a boxy distribution of the metal rich component, and the radial density gradient of the metal poor one is steeper. Due to the coarse spatial sampling of the GIBS fields, these maps have been derived imposing 4-fold symmetry (about the Galactic plane, and about the bulge projected minor axis). Therefore, we are by construction unable to identify possible asymmetries related to the fact that at positive (/negative) longitudes we see the near (/far) side of the bar.

Table 3. Components of the MDF fits and Nr of RC stars in each fields.

Field name	$\langle[\text{Fe}/\text{H}]\rangle$	σ	N/N_{tot}	$\langle[\text{Fe}/\text{H}]\rangle$	σ	N/N_{tot}	$\langle[\text{Fe}/\text{H}]\rangle$	σ	N/N_{tot}
		Halo			Metal poor			Metal rich	
LRp8p4	-1.38	0.08	0.02	-0.30	0.31	0.54	0.24	0.17	0.44
LRp5p4	–	–	0.00	0.04	0.34	0.27	0.49	0.09	0.73
LRp0p4	-1.14	0.08	0.02	-0.31	0.27	0.56	0.19	0.18	0.42
LRm3p4	-1.05	0.15	0.03	-0.35	0.23	0.34	0.24	0.24	0.63
LRm8p4	-0.91	0.13	0.02	-0.47	0.20	0.47	0.16	0.21	0.50
LRp0m1	-1.83	0.25	0.00	-0.35	0.28	0.53	0.22	0.18	0.46
LRp8m2	–	–	0.00	-0.87	0.12	0.03	0.00	0.34	0.97
LRp3m2	-1.40	0.16	0.01	-0.23	0.24	0.43	0.36	0.18	0.56
LRp0m2	-0.95	0.13	0.04	-0.26	0.29	0.56	0.37	0.19	0.40
LRm5m2	–	–	0.00	-0.30	0.20	0.35	0.24	0.17	0.65
LRm8m2	-1.42	0.12	0.01	-0.29	0.24	0.43	0.17	0.17	0.56
HRp8m3	–	–	0.00	-0.45	0.21	0.17	0.24	0.19	0.83
HRp4m3	-0.89	0.26	0.05	-0.18	0.19	0.41	0.32	0.15	0.54
BW	–	–	0.00	-0.23	0.39	0.48	0.33	0.16	0.52
HRm5m3	-1.60	0.06	0.01	-0.39	0.25	0.16	0.21	0.16	0.83
HRm7m4	-1.53	0.05	0.01	-0.45	0.16	0.29	0.22	0.21	0.70
LRp8m6	-1.27	0.30	0.03	-0.27	0.21	0.52	0.29	0.20	0.45
LRp4m6	-0.82	0.09	0.03	-0.26	0.22	0.40	0.28	0.22	0.57
bulge6	-0.90	0.31	0.09	-0.35	0.17	0.41	0.08	0.16	0.50
LRm4m6	-0.77	0.15	0.06	-0.35	0.17	0.41	0.23	0.22	0.52
LRm8m6	–	–	0.00	-0.36	0.36	0.94	0.26	0.17	0.06
LRp8m8	-1.00	0.06	0.02	-0.34	0.24	0.80	0.32	0.09	0.18
LRp4m8	-1.25	0.09	0.01	-0.35	0.26	0.59	0.31	0.17	0.41
LRp0m8	-0.85	0.54	0.04	-0.37	0.22	0.81	0.33	0.17	0.16
LRm3m8	-1.01	0.13	0.05	-0.35	0.24	0.82	0.36	0.11	0.13
LRm8m8	-1.01	0.18	0.07	-0.41	0.18	0.65	0.13	0.27	0.28
Global MDFs									
$b = -1^\circ$	-1.83	0.25	<0.01	-0.35	0.28	0.53	0.22	0.18	0.46
$b = -2^\circ$	-0.80	0.16	<0.02	-0.24	0.27	0.49	0.28	0.21	0.49
$b = -3.5^\circ$	-1.44	0.15	<0.01	-0.31	0.31	0.33	0.26	0.20	0.67
$b = +4^\circ$	-1.12	0.20	<0.02	-0.35	0.27	0.45	0.24	0.22	0.54
$b = -6^\circ$	-0.87	0.36	<0.06	-0.32	0.25	0.51	0.22	0.23	0.43
$b = -8.5^\circ$	-0.95	0.16	<0.04	-0.38	0.22	0.74	0.30	0.19	0.23

The two bulge metallicity components not only have different mean metallicity and different spatial distribution, they also have different kinematics. As already found by the BRAVA (Kunder et al. 2012) and the ARGOS survey (Ness et al. 2013b), in the outer bulge ($|b| > 4^\circ$) the metal poor component has a higher radial velocity dispersion compared to the metal rich one, at all longitudes. A new result of the present investigation is that this behaviour is reversed in the inner bulge. Specifically, at $b = -3.5^\circ$ and $b = -2^\circ$ the velocity dispersion of the metal poor stars becomes very similar to that of the metal rich ones, and at $b = -1^\circ$ it becomes smaller. This is due to the fact that the velocity distribution of the metal poor component has a mild gradient with latitude, ranging from $\sigma \sim 80$ km/s at $b = -8.5^\circ$ to $\sigma \sim 125$ km/s at $b = -1^\circ$. On the contrary, the metal rich component has a low velocity dispersion in the outer bulge ($\sigma \sim 60$ km/s at $b = -8.5^\circ$) that grows up to $\sigma \sim 145$ km/s at $b = -1^\circ$. In other words, the central *sigma-peak* discovered in Paper I, is mostly due to the metal rich stars. The origin of this *sigma-peak*, in the inner ~ 250 pc of the Galactic bulge, has been investigated by Valenti et al. (2016) who demonstrated that it coincides with a peak in the stellar density (traced by counting the number of RC stars across the VVV survey area) and thus with a peak in the mass density.

Finally, we investigated whether the GIBS data show any evidence for the metal poor component rotating slower than the metal rich one, as suggested by Kunder et al. (2015), who traced the former by means of RR Lyrae stars. Indeed, the metal poor component shows a marginally slower rotation also in the present dataset, although the difference is not compelling here.

Summarising, we unambiguously detect two components in the Galactic bulge, each having a relatively narrow metallicity distribution, so that the global bulge MDF is clearly bimodal. These two components have a different spatial distribution, with the metal poor being more centrally concentrated, and with a rounder density distribution as projected in the sky. On the contrary, the metal rich component is clearly boxy, as expected for a bar seen edge on. We stress that, although the present data are consistent with a spheroidal distribution of the metal poor component (although we did not investigate the 3rd component, along the line of sight), we are not presenting evidence in favor of it having a different origin (i.e., a *classical bulge*). Different models of bulge formation are being developed, arguing that a spheroidal shape can be obtained through different formation scenarios (Debattista, *priv. comm.*). We provide here new observational constraints that were not available so far, and need to be fulfilled by any Milky Way bulge formation model.

Acknowledgements. We gratefully acknowledge support by the Ministry of Economy, Development, and Tourism’s Millennium Science Initiative through grant IC120009, awarded to The Millennium Institute of Astrophysics (MAS), by Fondecyt Regular 1150345 and by the BASAL-CATA Center for Astrophysics and Associated Technologies PFB-06. This work was finalized at the Aspen Center for Physics, which is supported by National Science Foundation grant PHY-1066293. MZ and DM were partially supported by a grant from the Simons Foundation, during their stay in Aspen.

References

- Alard, C. 2001, *A&A*, 379, L44
- Alonso, A., Arribas, S., & Martínez-Roger, C. 1999, *A&AS*, 140, 261
- Alves-Brito, A., Meléndez, J., Asplund, M., Ramírez, I., & Yong, D. 2010, *A&A*, 513, A35+
- Athanassoula, E. 2005, *MNRAS*, 358, 1477
- Babusiaux, C. 2016, *PASA*, 33, e026
- Babusiaux, C., Katz, D., Hill, V., et al. 2014, *A&A*, 563, A15
- Dékány, I., Minniti, D., Catelan, M., et al. 2013, *ApJ*, 776, L19
- Gerhard, O. & Martínez-Valpuesta, I. 2012, *ApJ*, 744, L8
- Gonzalez, O. A., Rejkuba, M., Minniti, D., et al. 2011a, *A&A*, 534, L14
- Gonzalez, O. A., Rejkuba, M., Zoccali, M., et al. 2011b, *A&A*, 530, A54+
- Gonzalez, O. A., Rejkuba, M., Zoccali, M., et al. 2013, *A&A*, 552, A110
- Gonzalez, O. A., Rejkuba, M., Zoccali, M., Valenti, E., & Minniti, D. 2011c, *A&A*, 534, A3
- Gonzalez, O. A., Rejkuba, M., Zoccali, M., et al. 2012, *A&A*, 543, A13
- Gonzalez, O. A., Zoccali, M., Vásquez, S., et al. 2015, *A&A*, submitted
- Hartwick, F. D. A. 1976, *ApJ*, 209, 418
- Hill, V., Lecureur, A., Gomez, A., et al. 2011, *A&A*
- Howard, C. D., Rich, R. M., Clarkson, W., et al. 2009, *ApJ*, 702, L153
- Kunder, A., Koch, A., Rich, R. M., et al. 2012, *AJ*, 143, 57
- Kunder, A., Rich, R. M., Hawkins, K., et al. 2015, *ApJ*, 808, L12
- McWilliam, A. 2016, *PASA*, 33, e040
- McWilliam, A. & Rich, R. M. 1994, *ApJS*, 91, 749
- McWilliam, A. & Zoccali, M. 2010, *ApJ*, 724, 1491
- Minniti, D., Lucas, P. W., Emerson, J. P., et al. 2010, *New A*, 15, 433
- Minniti, D., Olszewski, E. W., Liebert, J., et al. 1995, *MNRAS*, 277, 1293
- Mucciarelli, A., Pancino, E., Lovisi, L., Ferraro, F. R., & Lapenna, E. 2013, *ApJ*, 766, 78
- Muratov, A. L. & Gnedin, O. Y. 2010, *ApJ*, 718, 1266
- Nataf, D. M., Udalski, A., Gould, A., Fouqué, P., & Stanek, K. Z. 2010, *ApJ*, 721, L28
- Nataf, D. M., Udalski, A., Skowron, J., et al. 2015, *MNRAS*, 447, 1535
- Ness, M. & Freeman, K. 2016, *PASA*, 33, e022
- Ness, M., Freeman, K., Athanassoula, E., et al. 2013a, *MNRAS*, 430, 836
- Ness, M., Freeman, K., Athanassoula, E., et al. 2013b, *MNRAS*, 432, 2092
- Ness, M., Freeman, K., Athanassoula, E., et al. 2012, *ApJ*, 756, 22
- Ortolani, S., Renzini, A., Gilmozzi, R., et al. 1995, *Nature*, 377, 701
- Pagel, B. E. J. 1989, in *Evolutionary Phenomena in Galaxies*, ed. J. E. Beckman & B. E. J. Pagel, 201–223
- Pasquini, L., Avila, G., Blecha, A., et al. 2002, *The Messenger*, 110, 1
- Patsis, P. A., Skokos, C., & Athanassoula, E. 2002, *MNRAS*, 337, 578
- Pietrukowicz, P., Kozłowski, S., Skowron, J., et al. 2015, *ApJ*, 811, 113
- Ramírez, I. & Meléndez, J. 2005, *ApJ*, 626, 465
- Rich, R. M. 1988, *AJ*, 95, 828
- Rich, R. M., Origlia, L., & Valenti, E. 2007, *ApJ*, 665, L119
- Rich, R. M., Origlia, L., & Valenti, E. 2012, *ApJ*, 746, 59
- Rojas-Arriagada, A., Recio-Blanco, A., Hill, V., et al. 2014, *A&A*, 569, A103
- Saha, K. & Gerhard, O. 2013, *MNRAS*, 430, 2039
- Saito, R. K., Zoccali, M., McWilliam, A., et al. 2011, *AJ*, 142, 76
- Schultheis, M., Cunha, K., Zasowski, G., et al. 2015, *A&A*, 584, A45
- Stanek, K. Z., Mateo, M., Udalski, A., et al. 1994, *ApJ*, 429, L73
- Terndrup, D. M. 1988, *AJ*, 96, 884
- Udalski, A., Szymanski, M., Kubiak, M., et al. 2002, *Acta Astron.*, 52, 217
- Valenti, E., Zoccali, M., Gonzalez, O. A., et al. 2016, *A&A*, 587, L6
- Vásquez, S., Zoccali, M., Hill, V., et al. 2015, *A&A*, 580, A121
- Vásquez, S., Zoccali, M., Hill, V., et al. 2013, *A&A*, 555, A91
- Wegg, C. & Gerhard, O. 2013, *MNRAS*, 435, 1874
- Wegg, C., Gerhard, O., & Portail, M. 2015, *MNRAS*, 450, 4050
- Zoccali, M., Gonzalez, O. A., Vasquez, S., et al. 2014, *A&A*, 562, A66
- Zoccali, M., Hill, V., Lecureur, A., et al. 2008, *A&A*, 486, 177
- Zoccali, M., Renzini, A., Ortolani, S., et al. 2003, *A&A*, 399, 931
- Zoccali, M. & Valenti, E. 2016, *PASA*, 33, e025